

# Study of sdO models. Pulsation Analysis

C. Rodríguez-López<sup>1,2,3\*</sup>, A. Moya<sup>3</sup>, R. Garrido<sup>3</sup>, J. MacDonald<sup>4</sup>, R. Oreiro<sup>5</sup> and A. Ulla<sup>2</sup>

<sup>1</sup>Laboratoire d'Astrophysique de Toulouse-Tarbes, Université de Toulouse, CNRS, Toulouse 31400, France

<sup>2</sup>Departamento de Física Aplicada, Universidade de Vigo, Vigo 36310, Spain

<sup>3</sup>Departamento de Física Estelar, Instituto de Astrofísica de Andalucía-CSIC, Granada 18008, Spain

<sup>4</sup>University of Delaware, Department of Physics and Astronomy, Newark, DE 19716, USA

<sup>5</sup>Institute of Astronomy, Katholieke Universiteit Leuven, Celestijnenlaan 200D, 3001 Leuven, Belgium

Accepted 2009 Month dd. Received 2009 Month dd; in original form 2009 Month dd

## ABSTRACT

We have explored the possibility of driving pulsation modes in models of sdO stars in which the effects of element diffusion, gravitational settling and radiative levitation have been neglected so that the distribution of iron-peak elements remains uniform throughout the evolution. The stability of these models was determined using a non-adiabatic oscillations code. We analysed 27 sdO models from 16 different evolutionary sequences and discovered the first ever sdO models capable of driving high-radial order  $g$ -modes. In one model, the driving is by a classical  $\kappa$ -mechanism due to the opacity bump from iron-peak elements at temperature  $\sim 200,000$  K. In a second model, the driving result from the combined action of  $\kappa$ -mechanisms operating in three distinct regions of the star: (i) a carbon-oxygen partial ionization zone at temperature  $\sim 2 \cdot 10^6$  K, (ii) a deeper region at temperature  $\sim 2 \cdot 10^7$  K, which we attribute to ionization of argon, and (iii) at the transition from radiative to conductive opacity in the core of the star.

**Key words:** stars: oscillations – stars: variables: other

## 1 INTRODUCTION

Hot subluminal O-stars (hereafter sdOs) are evolved objects on the way to becoming low-mass white dwarfs. Most sdOs are thought to have an inert carbon-oxygen core, with the luminosity provided by helium and hydrogen burning shells. The wide ranges of surface parameters, from 40 to 100 kK for effective temperature ( $T_{\text{eff}}$ ) and 4.0 to 6.5 for surface gravity ( $\log g$ ), spreads sdOs across a broad region in the HR diagram, that is crossed by post Asymptotic Giant Branch (post-AGB), post Red Giant Branch (post-RGB) and post Extended Horizontal Branch (post EHB) single star evolutionary tracks. This degeneracy in evolutionary paths plus possible binary star formation scenarios hampers reliable determination of sdO origins. This situation is not helped by the wide variety in sdO spectra: While they share a common characteristic of a He II 4686Å line, a diversity of lines with different strengths of He I, He II and sometimes H are possible, rendering spectral classification an open issue (Jeffery et al. 1997; Ströer et al. 2007).

The spectral analysis and determination of physical parameters has the drawback of requiring the use of non-LTE atmospheric codes due to high effective temperatures,

which yielded disagreements in the largest existent studies (Dreizler et al. 1990; Thejll et al. 1994) until recently. Recent analyses of 130 sdOs by Ströer et al. (2007) and Hirsch & Heber (2008) showed that they segregate into two main groups regarding helium content: (1) *helium-deficient* sdOs with subsolar He abundances, no traces of carbon or nitrogen and a large spread in  $T_{\text{eff}}$  and  $\log g$ , and (2) *helium-enriched* sdOs with supersolar He abundances and C and/or N lines present, spreading between  $\sim 40$ -50 kK in  $T_{\text{eff}}$  and 5.5 to 6 in  $\log g$ . Group (1) sdOs are classified as post-EHB descendants of hot subdwarf B-stars (hereafter sdBs). To explain the origins of group (2) sdOs, the authors invoke different channels: (i) merger of two helium white dwarfs formed by binary evolution (Webbink 1984; Han et al. 2002), which explains the He enrichment, but does not quite reproduce the observed  $T_{\text{eff}}$ - $\log g$  distribution, (ii) non-canonical evolution of a single star that experiences a phase of mixing from the H-shell into the envelope while on the RGB (Sweigart 1997) and (iii) evolution of a RGB star whose envelope is almost completely stripped by Roche-lobe overflow in a binary, pre-emptying the He - core flash (Driebe et al. 1999). This last scenario has problems in explaining the observed metal enrichment. (See Ströer et al. (2007) and references therein for a thorough review of sdO formation mechanisms).

\* E-mail:crodrigu@ast.obs-mip.fr

Another way to attack the problem of untangling the different evolutionary scenarios proposed for sdOs, and in which this paper focuses, is the use of asteroseismological methods (provided, of course, that sdOs are pulsating stars). Asteroseismological analysis can yield information such as the mass of the star, envelope, and inner structure through the Brunt-Väisälä frequency and/or sound speed, as long as we can identify the oscillation modes present in the star.

The first theoretical exploration of the potential of sdOs as pulsators was carried out by Charpinet et al. (1997a). The stability analysis of full stellar sdO models corresponding to seven evolutionary sequences starting on the EHB found all sdO models stable.

The previous year, Charpinet et al. (1996) had theoretically predicted the pulsator behaviour of sdBs due to a  $\kappa$ -mechanism caused by iron enhancement in the envelope of the star. Since the observational confirmation of the first pulsating sdB star by Kilkenny et al. (1997), we now know of about forty of these stars (Oreiro et al. 2009) termed V361 Hya, or more commonly EC 14026 stars, which coexist in the same area of the HR diagram with non-pulsating sdBs. They cluster in  $T_{\text{eff}}$  at  $\sim 33\,000$  K and  $\log g \sim 5.8$  dex and show oscillations with typical periods in the range 80–200 s, which have been identified with low-degree and low-radial order  $p$ -modes. Today, the sdB variable stars also include the long period pulsators V1093 Her (Green et al. 2003) also excited by the same  $\kappa$  mechanism (Fontaine et al. 2003), a handful of hybrid pulsators (e.g. Oreiro et al. 2005) and a unique He-sdB star (Ahmad & Jeffery 2005). For more details on sdB stars we refer the reader to the excellent review by Østensen (2009).

The goal of the present work is to complete the observational search for sdO pulsators (Rodríguez-López, Ulla & Garrido 2007; Rodríguez-López et al. 2005; Rodríguez-López et al. 2004) that proceeded in the period 2003–2006, and which has yielded non-conclusive results. The thrilling discovery of the first sdO pulsator, SDSS J160043.6+074802.9, (abbreviated J1600+0748) by a team of South African astronomers (Woudt et al. 2006), gave real support to our theoretical exercise. The recent discovery of  $p$ -mode oscillations in sdO models that included radiative levitation of iron (Fontaine et al. 2008) is able to account for the the very fast multiperiodic oscillations observed in the range  $\sim 60$  to  $\sim 120$  s, hence establishing the same iron opacity mechanism found in sdB stars as responsible for sdO oscillations, and reinforcing the conclusion that radiative levitation and gravitational settling are two key ingredients in driving pulsations (Charpinet et al. 1997b; Charpinet, Fontaine & Brassard 2009).

Our aim is to investigate the possibility of driving pulsation modes in theoretical models of sdO stars – coming from fully evolutionary sequences – with the aid of a non-adiabatic oscillations code. Thus, sdO models were specifically built using the evolutionary code JMSTAR (Lawlor & MacDonald 2006 and references therein). The code was used to further evolve these sdO models to more advanced state of evolution, providing the tracks taken in the HR diagram. The sdO models are used as input to the  $G_{\text{raCo}}$  non-adiabatic oscillations code (Moya, Garrido & Dupret 2004; Moya & Garrido 2008), which predicts which oscillation modes of the models are excited.

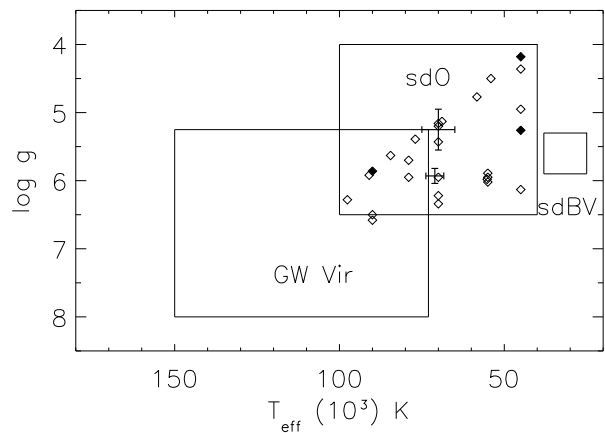


**Figure 1.** Diamonds mark the location of the sdO models in the  $\log g$ – $T_{\text{eff}}$  plane. Filled diamonds correspond to models 8, 10 and 15 which will be thoroughly described in following sections. The error bars give the  $T_{\text{eff}}$  and  $\log g$  determination for J1600+0748 by Fontaine et al. (2008) (bottom) and Rodríguez-López et al. (2009a) (top). A rough sketch of the sdO domain and the sdBV and GW Vir instability strips is also given.

The paper is structured as follows: In Section 2 we give some general remarks about the evolution code, the structural models and the non-adiabatic oscillations code. Section 3 briefly describes the non-adiabatic stability analysis carried on the sdO models. Sections 4, 5 and 6 describe the analysis for the most interesting models found. We summarise all the analysed models in Section 7, and the discussion and conclusions in Section 8.

## 2 THE TOOLS

### 2.1 The evolution code and the sdO models

To have accurate theoretical models of sdO stars is of great importance in the subsequent pulsation analysis. The distribution of the thermodynamical quantities, such as pressure, temperature, density, and the chemical composition in the interior of the star, will determine the theoretical spectrum of modes computed by the non-adiabatic oscillations code.

The evolution code JMSTAR was used to calculate a total of 16 initial sdO models corresponding to different evolutionary sequences (Table 1 shows some of their relevant properties). The models were built in a first step to account for the physical parameters of the pulsator sdOs candidates found in our simultaneous observational survey, and in a second step, trying to map out the sdO domain in the HR diagram. All of the models were created by evolving a  $1 M_{\odot}$  star, starting on the pre-Main Sequence. The initial metallicity is solar ( $Z = 0.02$ ) except models 7–9 for which  $Z = 0.05$ . The code follows the complete evolution of the star continuously to the sdO stage, and beyond. Fig. 1 roughly depicts the sdO domain in the HR diagram and the location of the constructed models. Their domain is located between the instability strips of the sdB variables and the GW Vir stars (low-degree  $g$ -mode pulsators excited by the C/O opacity mechanism)

**Table 1.** Main physical parameters and mass fractions of the sdO models (models named .1 means they belong to the same evolutionary sequence). X(other) refers to the mass fractions of all the other elements. Z is the current metallicity of the model (in brackets the initial metallicity, when different, at the ZAMS). Models between horizontal lines have been calculated with subtle differences in the code of evolution. (Model names are chosen mainly according to their mass loss rate parameter and effective temperature).

Model number & name	$T_{\text{eff}}$ (K)	$\log g$	M ( $M_{\odot}$ )	$\eta_{\text{R}}$	X(H)	X(He <sup>3</sup> )	X(He <sup>4</sup> )	X(C)	X(N)	X(O)	X(other)	Z
1 p675_8057	79 000	5.70	0.478	0.675	0.21	6.1E-05	0.72	3.4E-02	1.0E-02	5.2E-03	1.7E-02	0.07 (0.02)
1.1 p675_9065	90 000	6.50	0.478	0.675	0.20	5.4E-05	0.73	3.5E-02	1.0E-02	5.1E-03	1.7E-02	0.07 (0.02)
2 p650_7960	79 000	5.95	0.491	0.650	0.68	2.4E-04	0.30	3.0E-03	1.7E-03	1.0E-02	5.3E-03	0.02
3 etap 685	55 000	5.89	0.471	0.685	0.43	1.4E-04	0.55	9.6E-04	8.1E-03	5.6E-03	5.3E-03	0.02
4 etap 690	55 000	5.95	0.471	0.690	0.33	4.5E-05	0.65	6.3E-04	1.0E-02	4.0E-03	5.3E-03	0.02
5 etap 695	55 200	5.98	0.471	0.695	0.27	2.8E-05	0.71	9.0E-04	1.1E-02	3.2E-03	5.4E-03	0.02
6 etap 700	55 000	6.02	0.470	0.700	0.18	5.6E-05	0.78	1.5E-02	7.8E-03	2.6E-03	9.8E-03	0.04 (0.02)
7 eta 600t45	45 000	4.95	0.497	0.600	0.59	2.5E-04	0.36	7.3E-03	4.2E-03	2.4E-02	1.5E-02	0.05
7.1 eta 600t70	70 000	5.95	0.497	0.600	0.59	1.9E-04	0.35	7.3E-03	4.3E-03	2.4E-02	1.5E-02	0.05
8 eta 650t45	45 000	5.26	0.469	0.650	0.59	1.2E-03	0.35	7.4E-03	4.2E-03	2.4E-02	1.5E-02	0.05
8.1 eta 650t70	70 000	6.22	0.468	0.650	0.59	1.1E-03	0.36	7.4E-03	4.2E-03	2.4E-02	1.5E-02	0.05
9 eta 700t45	45 000	6.13	0.454	0.700	1.6E-03	8.2E-07	0.93	1.1E-02	2.7E-02	3.7E-03	2.7E-02	0.07 (0.05)
9.1 eta 700t70	70 000	6.34	0.453	0.700	1.63E-03	3.6E-07	0.93	1.1E-02	2.7E-02	3.7E-03	2.7E-02	0.07 (0.05)
10 eta 675t45mixi	45 000	4.18	0.479	0.675	0.26	5.2E-05	0.60	6.0E-02	9.5E-03	5.4E-02	1.7E-02	0.14 (0.02)
10.1 15773t54g45	54 500	4.54	0.479	0.675	0.24	4.3E-05	0.61	6.3E-02	9.7E-03	5.6E-02	1.7E-02	0.15 (0.02)
10.2 15873t58g47	58 300	4.68	0.479	0.675	0.24	4.1E-05	0.62	6.4E-02	9.8E-03	5.7E-02	1.7E-02	0.14 (0.02)
10.3 16973t69g51	69 000	5.14	0.479	0.675	0.19	2.4E-05	0.65	7.1E-02	1.0E-02	6.2E-02	1.9E-02	0.16 (0.02)
10.4 17773t77g54	77 000	5.39	0.479	0.675	0.16	1.4E-05	0.67	7.7E-02	1.1E-02	6.7E-02	2.0E-02	0.17 (0.02)
10.5 18273t84g56	84 500	5.63	0.479	0.675	0.13	9.0E-06	0.69	8.1E-02	1.1E-02	7.0E-02	2.1E-02	0.18 (0.02)
10.6 18573t91g59	90 700	5.93	0.479	0.675	0.11	5.9E-06	0.70	8.4E-02	1.2E-02	7.3E-02	2.1E-02	0.19 (0.02)
11 eta 675t45mixnmi	45 000	4.36	0.480	0	0.48	3.0E-04	0.45	2.8E-02	5.9E-03	2.9E-02	1.0E-02	0.07 (0.02)
12 eta 675t70mix1i	70 000	5.16	0.479	0.675	0.19	2.3E-05	0.65	7.1E-02	1.1E-02	6.2E-02	1.9E-02	0.16 (0.02)
13 eta 675t70mix2i	70 000	5.20	0.479	0.675	0.16	1.6E-05	0.66	7.5E-02	1.1E-02	6.6E-02	2.0E-02	0.18 (0.02)
14 eta 675t70mixnmi	70 000	5.43	0.480	0	0.48	3.0E-04	0.45	2.8E-02	5.9E-03	2.9E-02	1.0E-02	0.07 (0.02)
15 eta 675t90mixi	90 000	5.86	0.479	0.675	0.11	6.2E-06	0.70	8.4E-02	1.2E-02	7.3E-02	2.1E-02	0.19 (0.02)
15.1 18742t98g63	97 600	6.28	0.479	0.675	0.09	3.4E-06	0.71	8.8E-02	1.2E-02	7.6E-02	2.2E-02	0.20 (0.02)
16 eta 675t90mixnmi	90 000	6.58	0.480	0	0.48	3.0E-04	0.45	2.8E-02	5.9E-03	2.9E-02	1.0E-02	0.07 (0.02)

To obtain sdO models, the mass loss rate on the RGB is enhanced by a factor ranging from 1.60 to 1.85 compared to canonical Reimers' mass loss rates. Most of the hydrogen-rich envelope is removed just after or even before the helium core flash. At the highest RGB rates, the model stars leave the RGB and evolve to higher temperatures at constant luminosity, avoiding the AGB. They then suffer a helium-core flash just before or slightly after they enter a white dwarf cooling phase. After the core flash, the star is an EHB/sdB star burning He quiescently in the core. After core He exhaustion, the star enters the He shell burning sdO phase. The calculations are stopped when the model stars reach the (final) white dwarf phase. A born-again phase due to a very late thermal pulse occurs in some of the sequences. In this case, flash-driven convection carries nuclear processed material to the surface of the star, enriching the atmosphere with He, C, N and O. For particular models with sdO characteristics (see Table 1), we have performed a stability analysis.

The evolutionary tracks on which models 1–2, 3–6, 7–9 and 10–11 lie are depicted in Fig. 2, 3, 4 and 5. The complex evolution, near  $T_{\text{eff}} = 30\,000$  K ( $\log T_{\text{eff}} \sim 4.5$ ) in models 3 to 6, and in a wider range of temperatures for models 7–9, occurs near the end of the helium-core flash when the star is settling to a quiescent helium burning phase in the core, that is, the sdB phase. At the high mass loss rates used to

create models 3–6, the mass loss induced by the hot star wind is sufficient to expose internal He-rich layers. Thus, although the photospheres are not He-rich when the models reach the Horizontal Branch, they become He enriched due to the stellar wind as they evolve from sdBs to sdOs. Note that Fig. 2 shows only the part of the evolutionary tracks that occurs after the EHB phase.

There is an important difference between the evolutionary sequence of model 6 and the similar sequences of models 3–5. For model 6, the He-core flash occurs after the star has entered the white dwarf cooling phase, and in a similar manner to the evolution of post-AGB 'Born-Again' stars (see e.g. Lawlor & MacDonald 2006 and references therein), the convection zone that develops above the off-center He-burning region penetrates into the H-rich envelope. However, unlike the 'Born-Again' stars, this occurs when the He-burning region has become inactive and the temperature is too low for proton capture reactions to occur. The result of the mixing is to introduce  $\text{C}^{12}$  produced by the  $3\alpha$  process into the envelope, together with  $\text{O}^{18}$  and  $\text{Ne}^{22}$  produced by  $\text{N}^{14}$   $\alpha$ -captures. Shortly after the end of the He-core flash, this material is convected throughout the H-rich envelope, increasing the heavy element abundance to  $Z = 0.04$ . For models 3–5, the convection zone above the off-center He-burning region does not penetrate into H-rich envelope and there is no increase in the surface heavy element abundances. The

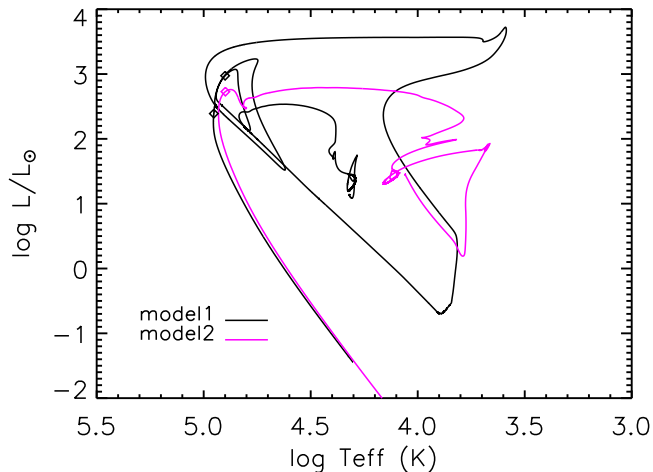


**Figure 2.** Evolutionary tracks from the horizontal branch described by models 1 and 2. A stability analysis was done also for a subsequent model in the evolutionary track of model 1, namely, model 1.1. Diamonds mark the location of the models.

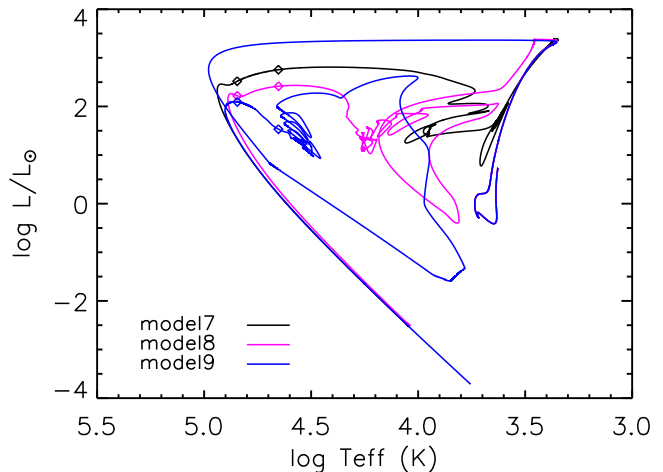


**Figure 4.** Complete evolutionary tracks for models 7–9. A stability analysis was done also for subsequent models in the evolutionary track, namely, models 7.1, 8.1 and 9.1. Diamonds mark the location of the six models.

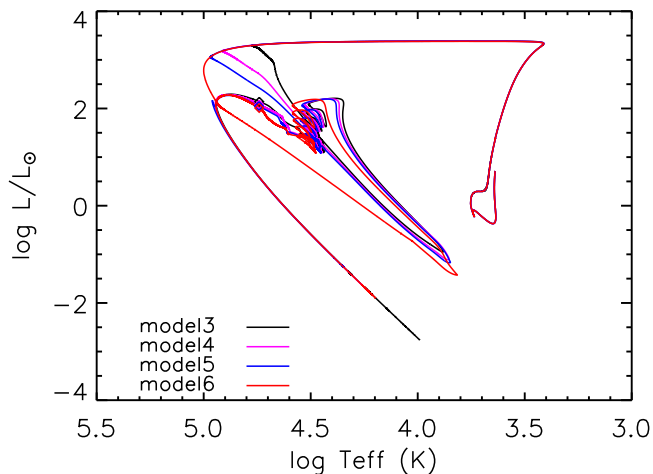


**Figure 3.** Complete evolutionary tracks for models 3–6. Diamonds mark the location of the models.

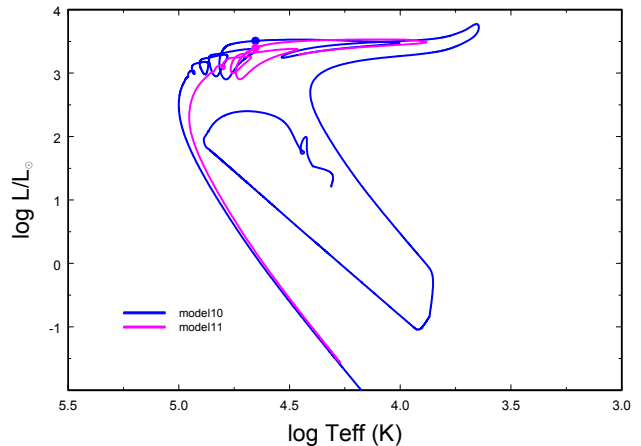


**Figure 5.** Evolutionary tracks from the horizontal branch for models 10 and 11. Dots mark the location of the models.

temporal evolution of the photospheric abundances for the model 6 sequence is shown in Fig. 6.

Models 10 to 16 require special comment. They are also late core helium flashers, but after they had arrived on the Zero Age Horizontal Branch (ZAHB) ad hoc extra-mixing was included for the purpose of bringing heavy elements to the surface to increase the envelope metallicity. Due to the extra-mixing, helium is also taken to higher temperatures, leading to helium shell flashes. Flash-driven convection then leads to further mixing of heavy elements to the surface. These helium shell flashes are responsible for the loops in Fig. 5, near  $T_{\text{eff}} \sim 60\,000$  K and  $\log g \sim 5$ . For models 11 (see Fig. 5), 14 and 16 mass loss was switched off in the calculations once they arrived on the ZAHB.

## 2.2 The oscillations code

We used the `GRACo` fully non-adiabatic oscillations code (Moya et al. 2004; Moya & Garrido 2008), which is based on

the Unno et al. (1989) formulation to study the sdO models described above. Because the thermal and dynamical time scales become comparable in the outer parts of the star, a non-adiabatic treatment of the oscillations is required in order to properly describe the dynamical characteristics of the oscillations, *i.e.* which modes will grow or decay with time. The non-adiabatic treatment does not significantly modify the eigenfrequencies with respect to the adiabatic, at least for our purposes, although it will modify the amplitudes and phases of the eigenfunctions. This proves to be very important in using multicolor photometry for mode identification of pulsating stars, although this is beyond the scope of this paper.

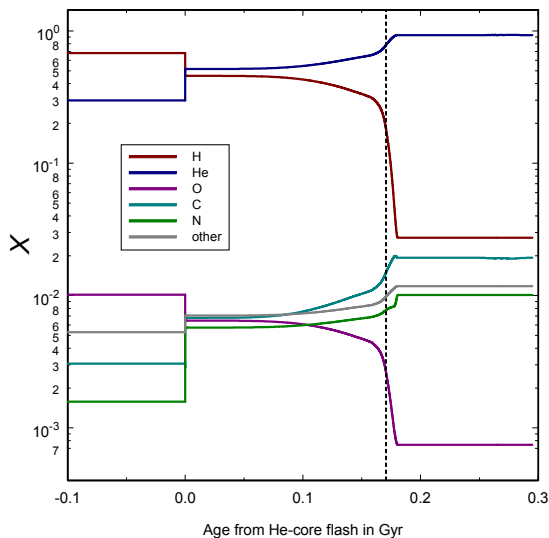


**Figure 6.** Temporal evolution of the photospheric abundances of the model 6 sequence. Time is measured from the peak of the He-core flash. The vertical line indicates the location of the sdO model 6.

### 3 NON ADIABATIC STABILITY ANALYSIS

We used `GRACo` to calculate modes from  $l = 0$  to  $l = 4$  with frequencies between  $\sim 0.3$  to  $\sim 20$  mHz ( $\sim 50$  to  $3000$  s), searching for excited short and/or long periods.

The stability or instability of a model is given by the growth rate as a function of the frequency. We used the Dziembowski, Moskalik & Pamyatnykh (1993) definition of the growth rate:  $\eta = W / \int_0^R |dW/dr| dr$  with the convention that positive (negative) values indicate driving (damping) of a particular mode.

In discussing which regions of the model contribute to driving or damping, we made use of the derivative of the work integral as a function of the fractional mass depth<sup>1</sup> ( $dW/d \log q$ ), which gives the energy locally gained or lost by the displaced material during one pulsation cycle. A positive (negative) value of  $-dW/d \log q$  at a given location indicates that this region contributes locally to driving (damping) a mode. Correspondingly, the running work integral ( $-W$ ) is also used to illustrate the relative importance of driving and damping zones.

In the next sections we describe the more interesting models found in the analysis.

### 4 MODEL 8: ETA 650T45

This model, taken from an evolutionary sequence with initial heavy element abundance  $Z = 0.05$ , has  $T_{\text{eff}} = 45\,000$  K and  $\log g = 5.25$ . Although it was found stable in the

<sup>1</sup> The fractional mass depth parameter  $\log q = \log(1 - M_r/M_T)$  gives a better resolution of the envelope structure, which is more relevant to pulsations than the structure of the deep interior.

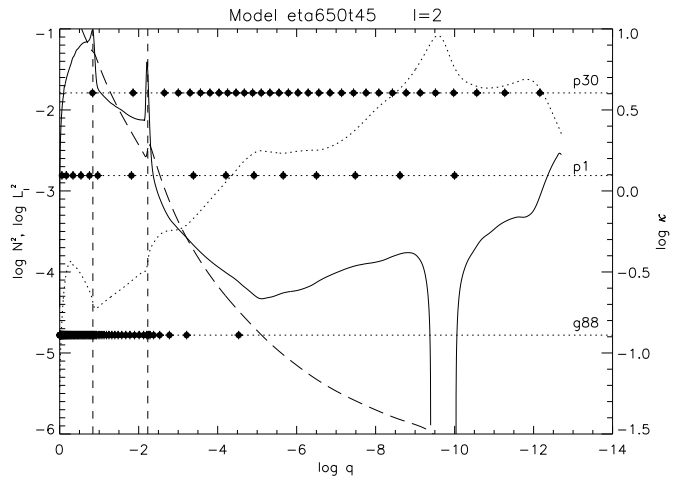


**Figure 7.** Propagation diagram: Brunt-Väisälä (solid line) and Lamb frequency (long-dashed line) for  $l = 2$  modes of model 8. The opacity (dotted line) scale is given in the right axis. The vertical dashed lines mark the maximum of the C/O-He and He-H chemical transitions. The frequencies of a pure  $g$ -mode ( $g88$ ), a mixed mode ( $p1$ ) and an almost pure  $p$ -mode ( $p30$ ) are given, with the positions of their nodes marked by circles. See text for further details.

whole frequency range, it has a narrow intermediate frequency region, corresponding to low-radial order  $p$ -modes, with a weak tendency to instability, which seemed interesting in terms of explaining a possible selection mechanism for observed modes in the only sdO pulsator found to date (Rodríguez-López et al. (2009b).

The model propagation diagram, representative of all the models used in the analyses, plus the opacity are shown in Fig. 7. There are three main bumps in the Rosseland opacity profile (scale given in the right axis): the shallowest at  $\log q \simeq -12$  corresponds to the helium ionization zone, where He II turns to He III at  $\sim 40\,000$  K; the maximum at  $\log q \simeq -9.5$ , which we will refer to as the Z-bump, is mainly due to iron-peak elements at  $\sim 200\,000$  K; and the one at  $\log q \simeq -5$  is the deep opacity bump at  $\sim 2\,000\,000$  K, which results from a combination of K-shell photoionization of carbon and oxygen and spinorbit effects in L-shell bound-free transitions of iron (Rogers & Iglesias 1992). It is clear from the opacity profile that the He II partial ionization zone is too high in the envelope to have any significant weight in the driving of the modes.

The Brunt-Väisälä ( $\log N^2$ ) and the Lamb frequencies ( $\log L_r^2$ ) are plotted for  $l = 2$ . The Brunt-Väisälä frequency has maxima where gradients in chemical composition are steepest. Hence, the peak at  $\log q \simeq -0.84$  accounts for the transition between the C/O core and the He burning shell, while the secondary peak at  $\log q \simeq -2.23$  is the transition between the radiative He and H burning shell. All the energy transport in the model is radiative except at  $-9.4 \leq \log q \leq -10.0$  where  $N^2 < 0$ , indicating that this is a convection zone associated with ionization of heavy elements producing an increase in the opacity rendering convective energy transport more efficient than radiation. We note here that models of sdB stars usually have a convective core and a radiative envelope with a thin convection zone produced by the partial ionization of HeII/HeIII (Charpinet et al. 2000).

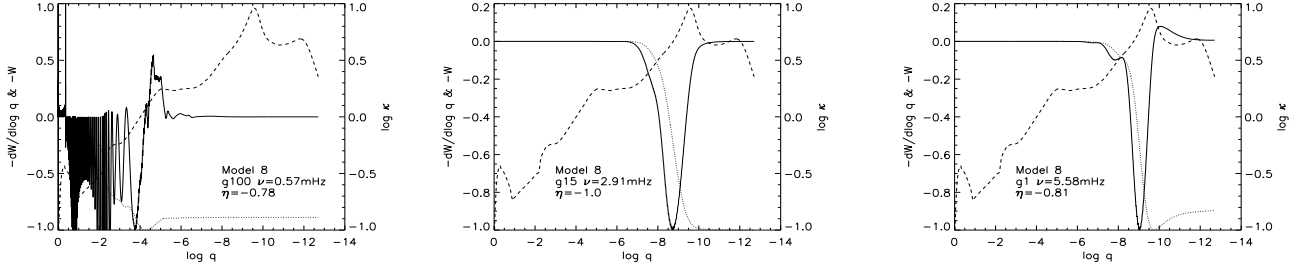


**Figure 8.** Left, Centre & Right: Differential work (solid line), running work integral (dotted line) and opacity (dashed line) for the  $g100$ ,  $g15$  and  $g1$  mode, respectively for a quadrupole mode of model 8. All plots have been scaled to arbitrary units.

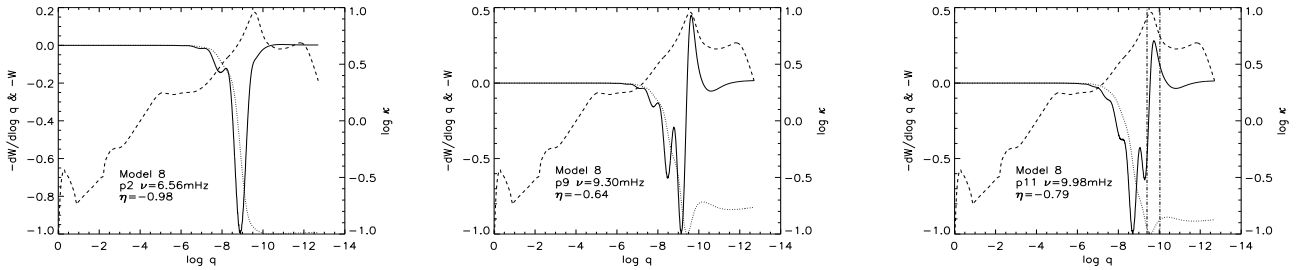


**Figure 9.** Left, Centre & Right: Differential work (solid line), running work integral (dotted line) and opacity (dashed line) for the  $p2$ ,  $p9$  and  $p11$  mode, respectively for a quadrupole mode of model 8. All plots have been scaled to arbitrary units. The vertical dashed-dotted lines in the last plot depict the convection zone.

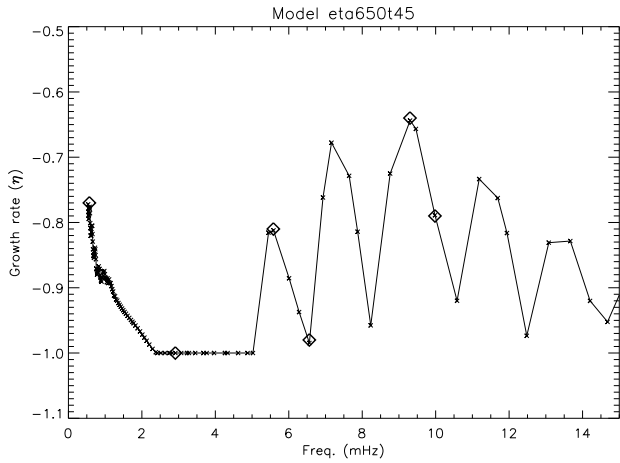


**Figure 10.** Growth rate vs. frequency for  $l = 2$  modes of model 8. Diamonds indicate the modes for which the differential work and running work integral were plotted.

The  $g$ - and  $p$ -mode propagation zones are determined respectively by  $\sigma^2 < N^2, L_l^2$  and  $\sigma^2 > N^2, L_l^2$ , with  $\sigma$  being the real part of the eigenfrequency. Fig. 7 shows that  $g$ -modes cannot propagate in the outer envelope, and that  $p$ -modes cannot propagate in the innermost part of the star, except for modes with very high-radial order<sup>2</sup>. The diagram also gives broad constraints on the range of frequencies in which modes can propagate. It gives an upper limit for the

angular frequencies of  $g$ -modes,  $\log \sigma^2 \lesssim -1$  – depending somewhat on the degree  $l$  – corresponding to cyclic frequencies  $\nu \lesssim 50$  mHz or periods  $P \gtrsim 20$  s. In the case of  $p$ -modes it gives a lower limit for eigenfrequencies,  $\log \sigma^2 \gtrsim -4.3$ , which translates to cyclic frequencies  $\nu \gtrsim 1.1$  mHz or periods  $P \lesssim 890$  s. Hence modes with oscillation eigenfrequencies in the range  $-4.3 \lesssim \log \sigma^2 \lesssim -1$  are mixed modes, i.e. they behave as  $p$ -modes in the outer part of the star and as  $g$ -modes in the inner zones. These limits correspond to a range in the frequency propagation of  $1.1 \lesssim \nu \lesssim 50$  mHz or a range in periods of  $20 \lesssim P \lesssim 890$  s. These mixed modes are typical of evolved stars, like sdOs, and hamper the identification of the modes: P and G modes' propagation zones are not separated by an evanescent zone, but their frequency ranges overlap significantly, as derived above. We should then be cautious about the nomenclature and emphasise that whenever we refer to a  $p$ - ( $g$ -) mode, we refer in fact to mixed modes with nodes mainly in the P (G) mode propagation zone (see position of nodes for modes  $p1$ ,  $p30$  in Fig. 7); except for those with high-radial orders (see nodes for mode  $g88$  in Fig. 7) i.e.  $g$ -modes with  $\nu \lesssim 1.1$  mHz, and  $p$ -modes with  $\nu \gtrsim 50$  mHz, far out of the frequency range considered here. In practice, for this model, modes with  $\nu \gtrsim 22$  mHz (or  $k > 33$ ) do not have modes in the G mode region.

We plot the growth rate  $\eta$  vs. frequency for  $l = 2$  modes (the behaviour being analogous for any degree  $l$ ) in Fig. 10, up to 15 mHz, as higher frequencies were found highly stable. The model is stable as the growth rate is negative in the whole frequency range. However there are 3 regions of interest in regard to stability:

- between about 0.5 to 1 mHz, where modes are not completely stable

<sup>2</sup> The radial order, represented by  $k$ , or sometimes  $n$ , gives the number of nodes of each mode, in the radial direction.

- from about 2.5 to 5 mHz, a highly-stable region
- from  $\sim 5$  mHz to 15 mHz, where the growth rate shows an oscillatory behaviour.

The differential work ( $-dW/d \log q$ ), running work integral ( $-W$ ), and opacity, for six modes (marked with diamonds in Fig. 10) chosen to be representative of the growth rate profile, give some insight into the local contributions and their relative importance to the work integral.

Fig. 8 shows the  $g100$  mode (on the left) with  $\nu = 0.57$  mHz and  $\eta = -0.78$ , which is representative of the low frequency region where the growth rate is not so negative. We identify a driving region at the location of the deep opacity bump as responsible for the not complete stabilization of the modes. However, due to the large number of nodes in the deepest region, radiative damping exceeds driving and the modes are stable.

The  $g15$  mode (centre) with  $\nu = 2.91$  mHz and  $\eta = -1$  represents the high-stability region found at frequencies between 2.5–5 mHz. The region where maximum energy interchange for the model occurs where the ratio of the dynamical to thermal timescales is  $\sim 1$  (corresponding to  $\log q \simeq -10$ ). For low-radial-order  $g$ -modes, maximum energy interchange takes place at  $\log q \simeq -9$ , where the derivative of the opacity does not favour driving, yielding a complete stabilization of the modes.

The onset of the oscillatory behaviour is represented by the  $g1$  mode (right) with  $\nu = 5.58$  mHz and  $\eta = -0.81$ . The mode gains a bit in instability due to the development of a weak driving region at  $-9.5 \lesssim \log q \lesssim -10$ , i.e. the Z-bump location. Its oscillating nature is due to the rise and fall of a driving zone at this Z-bump location, as we show next.

We plot 3 modes belonging to the third region of stability in Fig. 9. On the left panel, we plot  $p2$  mode with  $\nu = 6.56$  mHz and  $\eta = -0.98$ . We see that the reason for the low value of the growth rate is the vanishing driving region, whereas all the remaining energy contributes to damping.

The mode with maximum growth rate is  $p9$  (centre) with  $\nu = 9.30$  mHz and  $\eta_{\max} = -0.64$ . The reason is the maximum developing of the driving region at the location of the Z-bump.

The decrease of the growth rate at high frequencies is due to the energy damping region becoming wider and wider, as is the case for the  $p11$  mode (right) with  $\nu = 9.98$  mHz and  $\eta = -0.79$ .

Thus, the interplay between the development and extinction of a driving region at the Z-bump location is responsible for the oscillatory behaviour of the growth rate.

In an attempt to thoroughly investigate the properties of this model (and in particular the peculiar behaviour of the growth rate), we explored the behaviour of the kinetic energy of the modes. This led to the discovery of a mode trapping structure in the  $g$ - and  $p$ -mode spectra, the details of which will be presented elsewhere (Rodríguez-López et al. 2009b).

## 5 MODEL 10: ETA 675T45MIXI

This is the first of seven models – models 10 to 16, see Table 1 – created by introducing an artificial extra-mixing in the post-ZAHB evolution with the purpose of raising the

metallicity in the envelope in an attempt to drive pulsations, as explained in Section 2.1.

Model 10 was our first model discovered to be unstable. We found that high-radial order  $g$ -modes are driven through the action of a  $\kappa$ -mechanism due to the Z-bump at  $\sim 200,000$  K, the same mechanism that drives oscillations in sdB stars. Although the extra-mixing has significantly increased the abundances of C and O in the driving region, this has very little effect on the opacity there. Hence the presence of instability in this model shows that radiative levitation of iron is not a necessary condition for pulsations of sdO stars, as long as the metallicity is sufficiently increased. More evolved models from this evolutionary sequence (models 10.1 - 10.6 in Table 1) were also tested for pulsational instability. We found pulsations were driven in models with  $T_{\text{eff}} \leq 54,000$  K and  $\log g \leq 4.5$ . So, the instability strip for this evolutionary sequence was found to be  $45,000 \leq T_{\text{eff}} \leq 54,000$  K and  $4.2 \leq \log g \leq 4.5$ , and may extend to lower temperature and surface gravity.

The evolutionary track on the  $\log g$ - $T_{\text{eff}}$  diagram described by the time evolution of the model is shown in Fig. 11. The positions of the initial model 10 and the subsequent model found unstable are marked with diamonds. Crosses indicate intermediate structural models found stable in the stability analysis. The whole evolutionary time for this model is about 300,000 yr, while e-folding times of the excited modes are of the order of  $10^{-1}$  to 10 yr, so modes have enough time to grow in amplitude.

The growth rate profile for  $l = 2$  modes is shown in Fig. 12. We found two regions with excited modes (similar growth rate profiles and instability regions where found for the other degrees):

- within the frequency range  $0.29 \leq \nu \leq 0.32$  mHz (periods 52–58 min), which correspond to modes from  $g203$  to  $g182$  and
- within the frequency range  $0.38 \leq \nu \leq 0.42$  mHz (periods 40–44 min), which correspond to modes from  $g152$  to  $g138$

These modes fall within a wider range favoured for instability between  $0.2 \lesssim \nu \lesssim 1$  mHz. Meanwhile, modes with frequencies  $\nu \gtrsim 2$  mHz were found highly stable with  $\eta = -1.0$ . We have selected a few representative modes, marked with diamonds in Fig. 12, for further discussion. The profiles of the differential work, running work integral, and opacity for these representative modes are shown in Fig. 13.

We chose the  $g190$  mode with  $\nu = 0.31$  mHz and  $\eta = 0.17$  (Fig. 13, left) as representative of the two ‘islands’ of instability. There is a wide driving zone centered at  $\log q \simeq -8$ , the location of the Z-bump responsible for the instability.

To represent the stability zone between the two ‘islands’ of instability and, moreover, the stability zone up to 2 mHz, we chose the  $g177$  mode (Fig. 13, centre) with  $\nu = 0.33$  mHz and  $\eta = -0.95$ . The stability is due to the near extinction of the previous driving region and most of the significant energy contributing to damp the modes. The development and extinction of the region contributing to driving (with its maximum taking place at the location of the Z-bump) at the expense of a damping region is produced in the frequency range between  $\sim 0.2$  to 1.5 mHz and is responsible for the oscillatory profile of the growth rate.

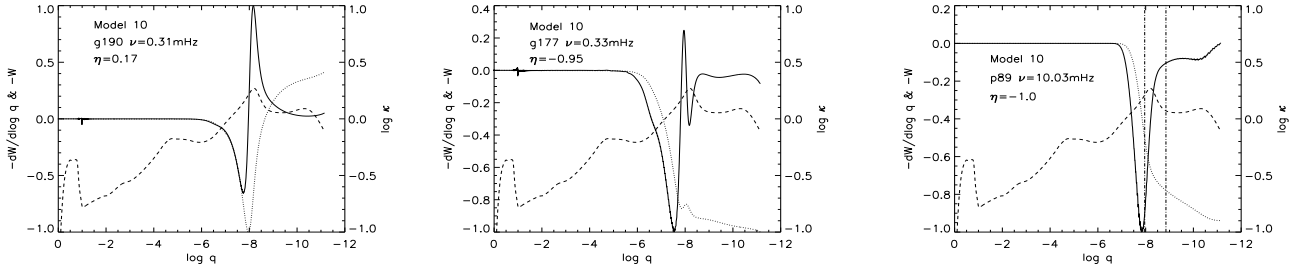


**Figure 13.** Left, Centre & Right: Differential work (solid line), running work integral (dotted line) and opacity (dashed line) for the  $g_{190}$ ,  $g_{177}$  and  $p_{89}$  mode, respectively for a quadrupole mode of model 10. All plots have been scaled to arbitrary units. The vertical dashed-dotted lines in the right plot depict the convection zone.

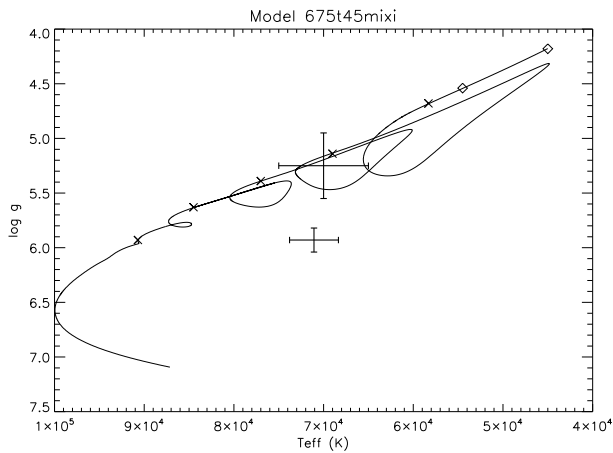


**Figure 11.** Evolutionary track described by model 10 (initial diamond). Diamonds mark models found unstable and crosses those found stable. Error bars give the  $T_{\text{eff}}$  and  $\log g$  determination for J1600+0748 by Fontaine et al. (2008) (bottom) and Rodríguez-López et al. (2009a) (top). Extra mixing in the model carries helium to hotter regions it burns giving rise to thermal pulses. The energy produced causes the star to expand and cool evolving to lower temperatures and when the burning finishes the star returns to higher temperatures.

Finally, mode  $p_{89}$  (Fig. 13, right) with  $\nu = 10.03$  mHz and  $\eta = -1.0$  is representative of the high stability of low and high-radial order  $p$ -modes. The stability is due to a wide damping region at the location of the Z-bump.

Model 10.1 of this same evolutionary sequence was found unstable in the frequency range (for  $l = 2$ , and similarly for other degrees):

- 0.71 to 0.75 mHz (periods 22-23 min) which corresponds to modes from  $g_{81}$  to  $g_{76}$ .

## 6 MODEL 15: ETA 675T90MIXI

This is the second model found unstable in our study. We found it drives two overstable modes. This driving is achieved through the action of three different driving regions: (i) the opacity bump at  $\sim 2,000,000$  K which for this model is due to a combination of opacity from iron-peak elements and, because of their increased abundances due to the extra-mixing, opacity from C and O, (ii) a driving

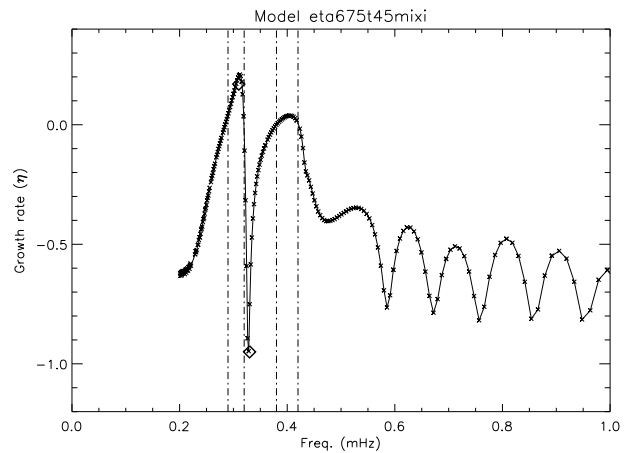


**Figure 12.** Growth rate vs. frequency for model 10. Diamonds indicate the modes for which the differential work and running work integral were plotted. The dashed-dotted lines delimit the two region of unstable modes. Higher frequency modes were found highly stable and were not plotted for clarity reasons.

region at  $\sim 2 \cdot 10^7$  K, located immediately above the hydrogen burning shell, and most likely due to the K-edge of highly ionised argon (Rogers & Iglesias 1992), and (iii) an opacity bump that occurs at the transition from radiative to conductive energy transport. At the high temperatures and densities in the core the radiative opacity is dominated by free-free absorption. Because the core temperature gradient is relatively small, the radiative opacity increases with the density. On the other hand the electrons become more degenerate with increasing density and the conductive opacity decreases. The combination of these two opacity variations gives a maximum in the opacity, corresponding to the opacity bump in driving region (iii) (see Fig. 18). Tests cancelling out the contribution of the nuclear energy generation show that the  $\epsilon$  mechanism is not responsible for this deepest driving region, nor for region (ii). The instability was obtained for  $l = 2$  modes (similar for other modes with other degrees):

- $g_{27}$  with  $\nu = 2.08$  mHz and  $\eta = 0.07$  and
- $g_{24}$  with  $\nu = 2.32$  mHz and  $\eta = 0.05$ .

This corresponds to periods in the range 7–8 min. Model 15 has one of the lowest H mass fraction, and one of the largest He, C and O mass fractions (see Table 1), which extend with constant values from the surface of the



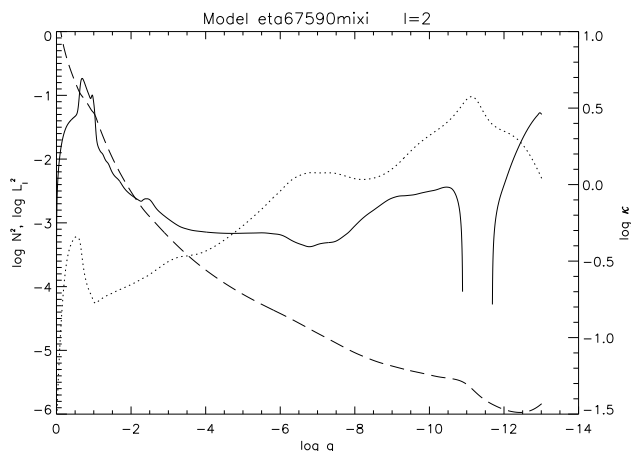


**Figure 14.** Brunt-Väisälä (solid line), Lamb frequency for  $l = 2$  and opacity (dashed line) for model 15. Both in units of  $\sigma^2$ .

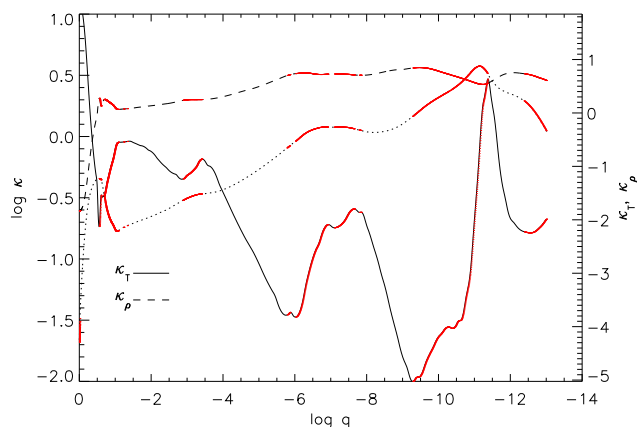


**Figure 15.** Rosseland mean opacity  $\kappa$  (dotted line, left axis), and its opacity derivatives (right axis):  $\kappa_T$  (solid line) and  $\kappa_\rho$  (dashed line). Red regions fulfil the criterion for instability. See text for details.

star down in the envelope until about  $\log q \simeq -4$ . It has also the largest metallicity,  $Z=0.19$ , of the whole series of models.

The propagation diagram and opacity of model 15 (Fig. 14) shows that the region of mixed modes is reduced compared to that of model 8, which is representative of most of the models used in this study. We also note that the Z-bump has shifted to shallower regions, with its maximum at  $\log q \simeq -11$  compared to  $\log q \simeq -10$  for the models with  $T_{\text{eff}} = 70\,000$  K or  $\log q \simeq -8$  for models with  $T_{\text{eff}} = 45\,000$  K.

A plot of the Rosseland mean opacity and its opacity derivatives,  $\kappa_T = \partial \ln \kappa / \partial \ln T|_\rho$  and  $\kappa_\rho = \partial \ln \kappa / \partial \ln \rho|_T$  is shown in Fig. 15. Opacity derivatives play an important role in the  $\kappa$  mechanism as the necessary condition for driving is given by the expression (Unno et al. 1989):

$$\frac{d}{dr} \left( \kappa_T + \frac{\kappa_\rho}{\Gamma_3 - 1} \right) > 0 \quad (1)$$

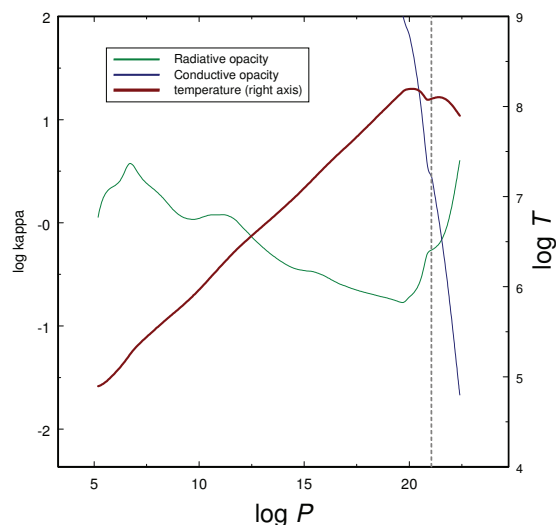


**Figure 18.** Radiative (green) and conductive (blue) opacity vs. pressure. Temperature (maroon) is given in the right axis. The vertical dashed line marks the opacity maximum. See text for details.

Regions in the star fulfilling this criterion are shown in red in Fig. 15. All the regions involved in the effective driving of the two excited modes are potential driving regions, together with the region of the Z-bump, also involved in the  $p$ -mode excitation (see below) and the very surface of the star, which, on the contrary, has no significant weight in the driving.

The age of this model from when it first became an sdO is about 10 000 yr, which is less than the linear growth rate e-folding times found:  $7 \cdot 10^4$  and  $10^5$  yr for  $g_{24}$  and  $g_{27}$ , respectively. However, the effective temperature remains near 90 000 K for more than  $10^5$  yr after this particular model. Therefore, from the rate of change of the effective temperature, the evolutionary time scale for this model is about  $10^5$  yrs, and modes may be able to develop observable amplitudes.

The normalised growth rate of the model is given in Fig. 19. It has a low frequency region with  $0.5 \lesssim \nu \lesssim 3.0$  mHz where the two overstable modes are driven, and in which high and low values of the growth rate alternate for consecutive modes. There is a highly stable region at intermediate frequencies  $5.0 \lesssim \nu \lesssim 13.0$  mHz and finally, a tendency to driving is found in the high frequency range with  $14.0 \lesssim \nu \lesssim 20$  mHz where low-radial order  $p$ -modes are found.

An example of a quasi-unstable mode in the very low frequency region, below 1 mHz, is given in Fig. 16 (left) by the  $g_{63}$  mode with  $\nu = 0.93$  mHz and  $\eta = -0.15$ . The high values of the growth rate are due to driving from region (i). At the high effective temperatures of this model this opacity bump occurs high in the envelope, at  $\log q \simeq -6$ , which favours pulsations, as heat interchange is more effective.

An example of a mode in the low frequency region which has lost its tendency to driving is given in Fig. 16 (centre) by the  $g_{35}$  mode with  $\nu = 1.63$  mHz and  $\eta = -0.72$ . In addition

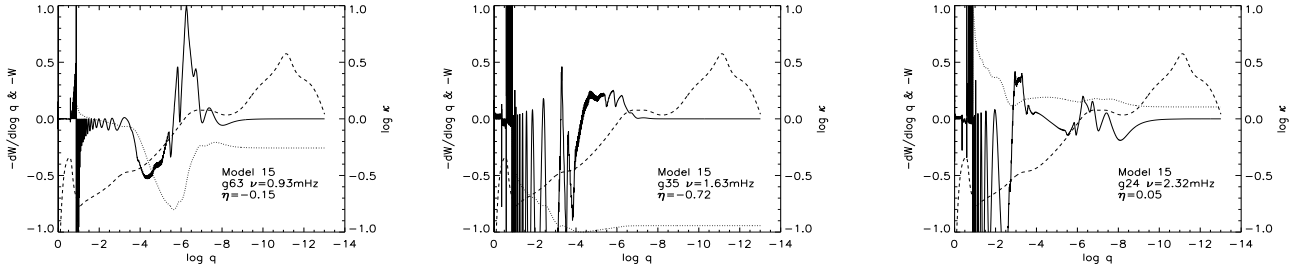


**Figure 16.** Left, Centre & Right: Differential work (solid line), running work integral (dotted line) and opacity (dashed line) for the  $g_{63}$ ,  $g_{35}$  and  $g_{24}$  mode respectively for a quadrupole mode of model 15. All plots have been scaled to arbitrary units.

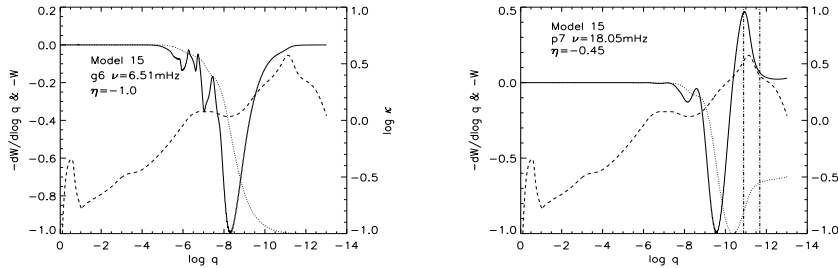


**Figure 17.** Left, & Right: Differential work integral (solid line), running work integral (dotted line) and opacity (dashed line) for the  $g_6$  and  $p_7$  mode respectively for a quadrupole mode of model 15. The vertical dashed-dotted lines in the right plot depict the convection zone. All plots have been scaled to arbitrary units.

to driving region (i), a driving region at  $-1 \lesssim \log q \lesssim -0.5$  (corresponding to  $\sim 8 \cdot 10^7$  K in temperature) has developed near the location of the deep opacity bump due to the transition from radiative to conductive energy transport in the semi-degenerate material. However, radiative damping right above this region exceeds the driving effect of both regions, damping the modes.

One of the two unstable modes found,  $g_{24}$  with  $\nu = 2.32$  mHz and  $\eta = 0.05$  is shown in Fig. 16 (right). A new driving region, which we attribute to Ar ionization, has developed at  $\log q \sim -3$ , where  $T \sim 210^7$  K. The model is able to achieve instability due to the combined driving of two of the three regions: the first and second, or the first and third regions, but modes are stable if only the first, or the joint second and third regions contribute to the differential work. It is the first time, to our knowledge, that driving of modes due to such a combined action of driving regions has been reported. This may give us a useful tool to explore physical processes, in particular energy transport, in dense hot regions.

A mode representative of the intermediate frequency region with the lowest values of the growth rate is the  $g_6$  mode with  $\nu = 6.51$  mHz and  $\eta = -1.0$  (Fig. 17, left). Modes at intermediate frequencies have maximum energy interchange at  $\log q \simeq -8.5$ , where the derivative of the opacity does not favour driving, which results in maximum stabilization of the modes.

Fig. 17 (right) shows mode  $p_7$  with  $\nu = 18.05$  mHz and  $\eta = -0.45$ , as an example of a quasi-unstable mode in the high frequency region where the low-radial order  $p$ -modes are found. This mode falls within the region of observed

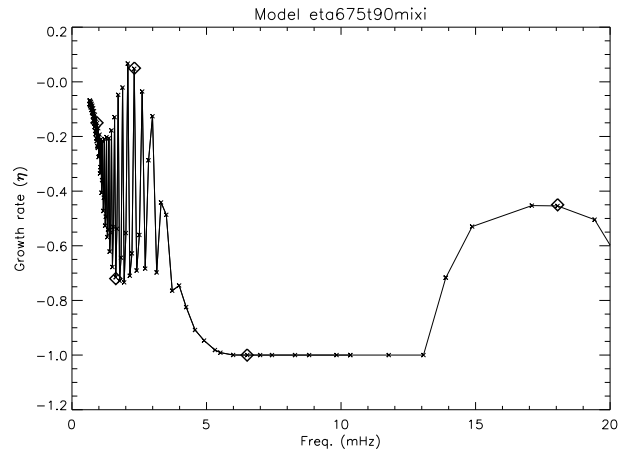


**Figure 19.** Growth rate vs. frequency for model 15. Diamonds indicate the modes for which the differential work and running work integral were plotted.

modes for J1600+0748. Surprisingly, due to the high  $T_{\text{eff}}$  of the model, the high values of the growth rate are due to a wide driving region caused by Z-bump. However, driving is not achieved as it is counterbalanced by a damping region located at the base of the Z-bump.

Further evolved models in the evolutionary sequence were analysed and found stable.

## 7 SUMMARY OF THE RESULTS

We present a summary of the stability analysis carried out for all the analysed models and submodels in Table 2. We give  $T_{\text{eff}}$ ,  $\log g$ , metallicity and if a tendency to instability – or actual instability – was found in the  $g$ - and/or  $p$ -mode spectrum and which driving region was responsible for it. In addition, we give the frequency and period range most favoured for instability.

If we draw our attention first to the first batch of models built for this study (models 1 to 9), all of them, except models 7 and 8, have a certain tendency to instability of the  $g$ -modes due to the gathering of driving energy at the location of the deep opacity bump at  $T \sim 2 \cdot 10^6$  K. This opacity bump is mainly due to iron-peak elements in models which have not experienced mixing of the products of core helium burning into the envelope. Opacity from C and O plays a role for models in which mixing has occurred. Whether or not opacity from C and O is important for driving, we label this driving region C/O in Table 2. Modes more favoured for driving are high-radial order  $g$ -modes, *i.e.* long period modes, with typical frequencies of oscillation between  $\sim 0.5$  and 2 mHz, *i.e.* periods  $\sim 500$  to 2000 s. We emphasize the unique behaviour of model 7 in which the tendency to instability of the  $g$ -modes is caused by the Z-bump.

We would expect that an increase in the C/O mass fraction, at least in the driving region, would lead to the eventual driving of the modes, as it is known that high metallicities help to increase the potential instability of the modes.

Models 1 and 8 have the Z-bump playing a role in the destabilization of the  $p$ -modes<sup>3</sup>. Model 8 presented an oscillatory profile of the growth rate with frequency, which lead us to analyse it in more detail, revealing mode trapping of  $g$ - and  $p$ -modes (Rodríguez-López et al. 2009b).

While doing this study we were aware that standard sdB evolutionary models with solar and uniform metallicities were not able to drive modes, and crude increases in the metallicity first (Charpinet et al. 1996) and the so-called second generation models next (Charpinet et al. 1997b) were needed to excite pulsations and reproduce theoretically the observed instability strip. The latter take diffusion (radiative levitation and gravitational settling) into account to produce a non-uniform profile of iron with depth, which is confirmed to be a key ingredient in driving pulsations (Charpinet et al. 2009).

Due to our negative results in exciting modes in this first batch of models, we aimed at building models as rich in metals as possible to test if it was possible to excite modes at some point via a  $\kappa$ -mechanism associated with a C/O partial ionization zone. Therefore, a last batch of models (models 10 to 16) was built in which an *ad hoc* extra-mixing was added to increase the metallicity in the envelope.

All these mixed-models have a tendency to driving of the high-radial order  $g$ -modes (see Table 2), caused by the Z-bump (this was only found previously for model 7), the C/O partial ionization zone, or a combination of both, the C/O being responsible for the tendency to driving of modes with lowest frequencies.

<sup>3</sup> Models marked with a lowercase z in Table 2 mean that the model barely reached the 'tendency to instability', considered as such when the growth rate values of the modes reach at least -0.5.

We finally achieved the instability of several models in the evolutionary sequence of model 10, that define a narrow instability band in the range  $45\,000 \leq T_{\text{eff}} \leq 54\,000$  K,  $4.2 \leq \log g \leq 4.5$ , metallicity  $0.14 \leq Z \leq 0.15$  and periods around 20 min, 45 min and 1 h. The instability is caused by a classical  $\kappa$ -mechanism due to the opacity bump of the iron-peak elements, that excite high-radial order  $g$ -modes in the star. Further time-evolved models in the same sequence were found stable.

Model 15, with  $T_{\text{eff}} = 90\,000$  K,  $\log g = 5.86$  and metallicity  $Z=0.19$ , was found to have unstable high-radial order  $g$ -modes due to driving from a combination of a classical  $\kappa$ -mechanism in the C/O partial ionization zone at  $T \sim 2 \cdot 10^6$  K, a  $\kappa$  mechanism operating at  $T \sim 2 \cdot 10^7$  K probably caused by argon ionization, and a  $\kappa$ -mechanism associated with an opacity bump that results from the transition from radiative to conductive opacities. This model has one of the largest total metallicity, helium, carbon and oxygen mass fractions within the whole set of models. We found it drives two overstable modes in the period range 7-8 min.

Models 10.5, 10.6 and 15, with temperatures between 84 500 and 91 000 K, show a tendency to instability of the low-radial order  $p$ -modes caused by the Z-bump. This behaviour is similar to that found in model 1, also a high temperature model ( $T_{\text{eff}} = 79\,000$  K). This is a somewhat unexpected result, as for such high  $T_{\text{eff}}$  the location of the Z-bump is quite high in the envelope of the star, where the driving efficiency is lower due to the lower density. Fortunately, this result is confirmed by actual driving of  $p$ -modes through a  $\kappa$  mechanism associated to the Z-bump is achieved by Fontaine et al. (2008) for two hot sdO models with  $T_{\text{eff}} = 71\,000$  and  $81\,000$  K, which include radiative levitation of iron. Those models have high temperatures fitting the first determination of physical parameters of J1600+0748,  $T_{\text{eff}} = 71\,000 \pm 2725$  K and  $\log g = 5.93 \pm 0.11$ , also derived by Fontaine et al. (2008).

## 8 DISCUSSION AND CONCLUSIONS

We carried out a non-adiabatic analysis of sdO equilibrium models to explore their feasibility as pulsators. We analysed 27 sdO models out of 16 different evolutionary sequences and we found the first two sdO evolutionary models ever to drive high-radial order  $g$ -modes. In one model, with  $T_{\text{eff}} = 45\,000$  K, instability of  $g$ -modes is due to a classical  $\kappa$ -mechanism in the partial ionization zone of the iron-peak elements at  $T \sim 2 \cdot 10^5$  K. This shows that radiative levitation is not an absolute pre-requisite for pulsations of a model sdO star as long as the metallicity is increased to what are probably unrealistic values. Inclusion of radiative levitation of iron remains necessary for complete asteroseismological analysis of hot subdwarfs. In the second model, with  $T_{\text{eff}} = 90\,000$  K,  $g$ -modes are found to be unstable due to the combination of driving from three distinct regions in the star. The outermost driving region is located at  $T \sim 2 \cdot 10^6$  K, where the iron-peak opacity bump is strongly augmented by contributions from ionization of carbon and oxygen, which we have enhanced in abundance by *ad-hoc* extra-mixing during the evolution after the ZAHB. The second driving region is located at  $T \sim 2 \cdot 10^7$  K where a subtle opacity bump develops due to the ionization of argon. The innermost driv-

**Table 2.** Effective temperature, logarithm of surface gravity, current metallicity and region responsible for the tendency to driving—or actual driving— of the  $g$ - and/or  $p$ -modes spectrum. The last two columns give the frequency or period range of most favoured for driving (taking into account modes from  $l = 1$  to  $l = 4$ ). The lower-case  $z$  for models 7 and 8 indicates the modes are under the limit of the tendency to driving. Models between horizontal lines have been calculated with small changes in the evolution code. Models in bold were found unstable.

Model number & name	$T_{\text{eff}}$ (K)	$\log g$	Z	$g$ -modes	$p$ -modes	Freq. range (mHz)	Period range (s)
1 p675_8057	79 000	5.70	0.07	C/O	Z	0.5–1.5, 10–14	700–2000, 70–100
1.1 p675_9065	90 000	6.50	0.07	C/O	–	0.5–5	200–2000
2 p650_7960	79 000	5.95	0.02	C/O	–	0.5–1	1000–2000
3 etap 685	55 000	5.89	0.02	C/O	–	0.5–2.5	400–2000
4 etap 690	55 000	5.95	0.02	C/O	–	0.5–2.5	400–2000
5 etap 695	55 200	5.98	0.02	C/O	–	0.5–3	300–2000
6 etap 700	55 000	6.02	0.04	C/O	–	0.5–2.5	
7 eta 600t45	45 000	4.95	0.05	$z$	–	2–5	200–500
7.1 eta 600t70	70 000	5.95	0.05	C/O	–	0.5–1.5	700–2000
8 eta 650t45	45 000	5.26	0.05	–	$z$	7–9.5	100–150
8.1 eta 650t70	70 000	6.22	0.05	C/O	–	0.5–3.5	300–2000
9 eta 700t45	45 000	6.13	0.07	C/O	–	1–7	150–1000
9.1 eta 700t70	70 000	6.34	0.07	C/O	–	0.5–4	250–2000
<b>10 eta 675t45mixi</b>	45 000	4.18	0.14	Z	–	0.2–0.9	1100–5000
<b>10.1 15773t54g45</b>	54 500	4.54	0.15	Z	–	0.3–2	500–3300
10.2 15873t58g47	58 300	4.68	0.14	Z	–	0.3–2.5	400–3000
10.3 16973t69g51	69 000	5.14	0.16	C/O+Z	–	0.2–3.5	300–5000
10.4 17773t77g54	77 000	5.39	0.17	C/O+ Z	–	0.2–1.5, 4–6.5	700–5000, 150–250
10.5 18273t84g56	84 500	5.63	0.18	C/O	Z	0.2–1, 8–11	1000–5000, 90–125
10.6 18573t91g59	90 700	5.93	0.19	C/O	Z	0.2–3, 17–21	300–5000, 50–60
11 eta 675t45mixnmi	45 000	4.36	0.07	Z	–	0.4–0.7	1400–2500
12 eta 675t70mixli	70 000	5.16	0.16	C/O + Z	–	0.2–1, 2.5–4	1000–5000, 250–400
13 eta 675t70mix2i	70 000	5.20	0.18	C/O + Z	–	0.2–0.5, 3–4	2000–5000, 250–300
14 eta 675t70mixnmi	70 000	5.43	0.07	C/O + Z	–	0.4–0.8, 5–7	1250–2500
<b>15 eta 675t90mixi</b>	90 000	5.86	0.19	C/O	Z	0.3–3.5, 15–20	300–3300, 50–65
15.1 18742t98g63	97 600	6.28	0.20	C/O	–	1.5–2	500–700
16 eta 675t90mixnmi	90 000	6.58	0.07	C/O	–	2–4, 5.5–7	250–500, 150–180

ing region is located at the transition between radiative and conductive energy transport, and may be of interest as a tool to explore energy transport processes in dense hot regions.

All of our sdO models, except one, present a certain tendency to instability for high-radial order  $g$ -modes, with typical oscillation frequencies between  $\sim 0.5$  and 2 mHz (i.e. periods  $\sim 500$ –2000 s). For most of the models this tendency to driving is usually due to the occurrence of a driving zone at the location of the C/O partial ionization zone. However, quasi-excitation due to the heavy elements partial ionization zone or a combination of both also occurred.

The fact that we found actual driving due to a  $\kappa$ -mechanism associated with C/O opacity in only one model may be due to the deep location of the C/O partial ionization zone within the star, where the high ratio of the thermal to dynamical time scales impedes efficient heat interchange. Hence, only hotter models with shallower partial ionization zones, such as model 15 for which we achieved actual driving, may be able to overcome this problem.

The tendency to instability of  $p$ -modes was not so common, and was achieved for only 5 out of 27 models. We did not achieve actual driving of  $p$ -modes, those observed in the only sdO pulsator known to date, in any of our models. In some of the hotter models, we found a tendency to driving of low-radial order  $p$ -modes, always triggered by the

$\kappa$ -mechanism associated with the Z-bump. We partially attribute the inability to get actual  $p$ -mode driving to the shallow location of the heavy elements partial ionization zone, where the density is low, making its contribution to the work integral not sufficient to drive the modes. However, this difficulty has been now overcome by the results of Fontaine et al. (2008) who have achieved the actual driving of  $p$ -modes for hot models which include radiative levitation and gravitational settling of iron.

Finally, we would like to remark that, as shown by Fontaine et al. (2008) and Charpinet et al. (2009), inclusion of radiative levitation of iron in the models has revealed essential in achieving the actual excitation of  $p$ -modes. The determination of physical parameters (Fontaine et al. 2008; Rodríguez-López et al. 2009a) for the unique pulsating sdO star to date provides us with an excellent clue to pursue observational searches for new sdO pulsators, with the aim of characterising their instability strip. Envisaged problems are the lack of catalogued sdOs with high effective temperatures, as historically, atmosphere grids reached only up to about 55 000 K. The role of recent sky surveys such as the Sloan Digitally Sky Survey<sup>4</sup> and new tools as those offered by the

<sup>4</sup> <http://www.sdss.org/>

Virtual Observatory<sup>5</sup> are crucial for spectroscopic and photometric searches of new sdO candidates. The road ahead is challenging, as candidates will be mostly faint (magnitudes at least over 16 or 17) which will pose difficulties in achieving high S/N light curves that allow to detect the lowest amplitude modes. Strategies as propose sdO candidates to be observed by asteroseismologic satellites such as CoRoT or KEPLER have to be considered.

## ACKNOWLEDGMENTS

CRL acknowledges an *Ángeles Alvariño* contract of the regional government *Xunta de Galicia*. This research was also supported by the Spanish Ministry of Science and Technology under project ESP2004-03855-C03-01 and by the *Junta de Andalucía* and the *Dirección General de Investigación (DGI)* under project AYA2000-1559. AM acknowledges financial support from a *Juan de la Cierva* contract of the Spanish Ministry of Education and Science. RO is supported by the Research Council of Leuven University through grant GOA/2003/04.

## REFERENCES

- Ahmad A., Jeffery, C. S., 2005 A&A, 437, L51  
 Charpinet S., Fontaine G., Brassard P., Dorman, B., 1996, ApJ, 471, L103  
 Charpinet S., Fontaine G., Brassard P., Dorman, B., 1997a, ApJ, 489, L149  
 Charpinet S., Fontaine G., Brassard P., Chayer P, Rogers F. J., Iglesias C. A., Dorman B., 1997b, ApJ, 483, L123  
 Charpinet S., Fontaine G., Brassard P., Dorman, B., 2000, ApJS, 131, 223  
 Charpinet S., Fontaine G., Brassard P., 2009, A&A, 493, 595  
 Dreizler S., Heber U., Werner K., Moehler S., de Boer K. S., 1990, A&A, 235, 234  
 Driebe T., Blöcker T., Schönberner D., Herwig F., 1999, A&A, 350, 289  
 Dziembowski W. A., Moskalik P., Pamyatnykh A. A., 1993, MNRAS, 265, 588  
 Fontaine G., Brassard P., Charpinet S., Green E. M., Chayer P., Billères M., Randall S. K., 2003, ApJ, 597, 518  
 Fontaine G., Brassard P., Green E. M., Chayer P., Charpinet S., Andersen M., Portouw J., 2008, A&A, 486, L39  
 Green E. M. et al., 2003, ApJ, 583, L31  
 Han Z., Podsiadlowski Ph., Maxted P. F. L., Marsh T. R., Ivanova N., 2002, MNRAS, 336, 449  
 Hirsch H., Heber U., 2008, to appear in ASPC, vol. 392, Proceedings of the Hot Subdwarf Stars and Related Objects, p. 175  
 Jeffery C. S., Drilling J. S., Harrison P. M., Heber U., Moehler S., 1997, A&AS, 125, 501  
 Kilkeny D., Koen C., O'Donoghue D., Stobie R. S., 1997, MNRAS, 285, 640  
 Lawlor T. M., MacDonald J., 2006, MNRAS, 371, 263  
 Moya A., Garrido R., Dupret M.-A., 2004, A&A, 414, 1081  
 Moya A., Garrido R., 2008, Ap&SS, 316, 129  
 Oreiro R., Pérez-Hernández F., Ulla A., Garrido R., Østensen R., MacDonald J., 2005, A&A, 438, 257  
 Oreiro R., Østensen R. H., Green E. M., Geier S., 2009, A&A, 496, 827  
 Østensen R. H., 2009, to appear in Communications in Asteroseismology vol.159, Proceedings of the JENAM 2008 Symposium No 4: Asteroseismology and Stellar Evolution  
 Rodríguez-López C., Ulla A., Garrido R., Manteiga M., Thejll P., 2004, Ap&SS, 291, 431  
 Rodríguez-López C., Ulla A., Garrido R., Manteiga M., Casanova V., Sota A., Østensen R., Oreiro R., 2005, in Koester D., Moehler, S., eds., ASP Conf. Ser. Vol. 334, 14th European Workshop on White Dwarfs. Astron. Soc. Pac., San Francisco, p. 627  
 Rodríguez-López C., Ulla A., Garrido R., 2007, MNRAS, 379, 1123  
 Rodríguez-López C. et al., 2009a, MNRAS, accepted, (astro-ph/0909.0930)  
 Rodríguez-López C., Moya A., Garrido R., MacDonald J., Oreiro R., Ulla A. 2009b, in preparation  
 Rogers F. J., Iglesias C., 1992, ApJS, 79, 50  
 Ströer A., Heber U., Lisker T., Napiwotzki R., Dreizler S., Christlieb N., Reimers D., 2007, A&A, 462, 269  
 Sweigart A., 1997, ApJ, 474, L23  
 Thejll P., Bauer F., Saffer R., Liebert J., Kunze D., Shipman H. L., 1994, ApJ433, 819  
 Unno W., Osaki Y., Ando H., Saio H., Shibahashi H., 1989, Nonradial Oscillations of stars, Tokyo: University of Tokyo Press, 2nd ed.  
 Webbink R. F., 1984, ApJ, 277, 355  
 Woudt P. A. et al., 2006, MNRAS, 371, 1497

<sup>5</sup> <http://www.ivoa.net>